Monthly Notices of the ROYAL ASTRONOMICAL SOCIETY

MNRAS **527,** L42–L46 (2024) https://doi.org/10.1093/mnrasl/slad139
Advance Access publication 2023 September 27

Palomar discovery and initial characterization of naked-eye long-period comet C/2022 E3 (ZTF)

B. T. Bolin [1,2,3★†] F. J. Masci,[3] D. A. Duev,[4] J. W. Milburn,[5] J. D. Neill,[2,5] J. N. Purdum,[5] C. Avdellidou [6,14] M. Saki,[7,8] Y.-C. Cheng,[9,10] M. Delbo,[6] C. Fremling,[2,5] M. Ghosal [11] Z.-Y. Lin,[12] C. M. Lisse[13] and A. Mahabal [2]

[1]*Goddard Space Flight Center, 8800 Greenbelt Road, Greenbelt, MD 20771, USA*
[2]*Division of Physics, Mathematics and Astronomy, California Institute of Technology, Pasadena, CA 91125, USA*
[3]*Infrared Processing and Analysis Center, California Institute of Technology, Pasadena, CA 91125, USA*
[4]*Weights & Biases, San Francisco, CA 94103, USA*
[5]*Caltech Optical Observatories, California Institute of Technology, Pasadena, CA 91125, USA*
[6]*CNRS Lagrange, Observatoire de la Côte d'Azur, Université Côte d'Azur, Nice 06304, France*
[7]*Department of Physics, Edmund C. Leach Science Center, Auburn University, Auburn, AL 36849, USA*
[8]*Department of Mathematics, Physics, Astronomy, & Statistics, University of Missouri, St Louis, MO 63121, USA*
[9]*Department of Physics, National Taiwan Normal University, Taipei City 116325, Taiwan*
[10]*Center of Astronomy and Gravitation, National Taiwan Normal University, Taipei City 116325, Taiwan*
[11]*Institute for Astronomy, University of Hawai'i, 2680 Woodlawn Dr, Honolulu, HI 96822, USA*
[12]*Institute of Astronomy, National Central University, Taoyuan City 32001, Taiwan*
[13]*Johns Hopkins University Applied Physics Laboratory, 11100 Johns Hopkins Rd, Laurel, MD 20723, USA*
[14]*School of Physics and Astronomy, University of Leicester, Leicester LE1 7RH, United Kingdom*

Accepted 2023 September 22. Received 2023 September 21; in original form 2023 September 2

ABSTRACT

Long-period comets are planetesimal remnants constraining the environment and volatiles of the protoplanetary disc. We report the discovery of hyperbolic long-period comet C/2022 E3 Zwicky Transient Facility (ZTF), which has a perihelion ∼1.11 au, an eccentricity $\gtrsim$1 and an inclination ∼109°, from images taken with the Palomar 48-inch telescope during morning twilight on 2022 March 2. Additionally, we report the characterization of C/2022 E3 (ZTF) from observations taken with the Palomar 200-inch, the Palomar 60-inch, and the NASA Infrared Telescope Facility in early 2023 February to 2023 March when the comet passed within ∼0.28 au of the Earth and reached a visible magnitude of ∼5. We measure g–$r = 0.70 \pm 0.01$, r–$i = 0.20 \pm 0.01$, i–$z = 0.06 \pm 0.01$, z–$J = 0.90 \pm 0.01$, J–$H = 0.38 \pm 0.01$, and H–$K = 0.15 \pm 0.01$ colours for the comet from observations. We measure the A(0°)fρ (0.8 μm) in a 6500 km radius from the nucleus of 1483 ± 40 cm, and CN, C_3, and C_2 production of $5.43 \pm 0.11 \times 10^{25}$, $2.01 \pm 0.04 \times 10^{24}$, and $3.08 \pm 0.5 \times 10^{25}$ mol s^{-1}, similar to other long-period comets. We additionally observe the appearance of jet-like structures at a scale of ∼4000 km in wide-field g-band images, which may be caused by the presence of CN gas in the near-nucleus coma.

Key words: minor planets – asteroids: general.

1 INTRODUCTION

Long-period comets, defined as having an orbital period >200 yr, originate from the Oort Cloud, an isotropic reservoir of nuclei extending to 10 000s of au from the Sun (Oort 1950). It is modelled that the Oort cloud was created by the scattering of planetesimals in the original trans-Neptunian disc onto orbits with semi-major axes >10 000 au through close encounters with the gas giants (Duncan, Quinn & Tremaine 1987; Vokrouhlický, Nesvorný & Dones 2019). Interactions with galactic tides and encounters with passing stars can cause the perihelia of the scattered comets to cross the planetary region where they are scattered into the inner Solar system by planetary encounters (e.g. Dybczyński & Królikowska 2022).

While planetesimals in the original trans-Neptunian disc are thought to be initially formed as large 100 km-scale bodies (Klahr & Schreiber 2020; Simon et al. 2022), collisional evolution subsequent to their formation resulted in the production of collisional aggregates ≲10 km in size (Bottke et al. 2023). Therefore, the Oort Cloud was populated by many 10 km-scale or smaller bodies that have returned as long-period comets as detected by ground-based surveys (Boe et al. 2019) providing the opportunity to study the remnants of the original planetesimals.

The Palomar Observatory 48-inch (P48) telescope's Zwicky Transient Facility (ZTF) camera scans the observable night sky twice every night (Bellm et al. 2019) and has the capability of

★ E-mail: bolin.astro@gmail.com
† NASA Postdoctoral Program Fellow

observing asteroid and comet transients down to $V \sim 20$–21 (e.g. Bolin et al. 2021a, 2022a; Farnocchia et al. 2022). The ZTF survey time is divided between a general all-sky survey (Graham et al. 2019) and micro-surveys specifically designed to detect Solar system objects (Chang et al. 2022; Bolin et al. 2023b). Both survey types are processed with data analysis techniques designed to discovery and characterize asteroids and comets (Duev et al. 2019, 2021; Masci et al. 2019; Golovich et al. 2021). On 2022 March 2, a cometary object, C/2022 E3 (ZTF), was discovered in P48/ZTF images taken during morning twilight (Bolin et al. 2022b).

Operation of telescopes such as the Palomar 60-inch telescope (P60), Palomar 200-inch (P200), and the Infrared Telescope Facility have been used to follow up and characterize asteroids and comets observed by the P48-inch (Bolin et al. 2020a; Purdum et al. 2021; Bolin et al. 2023d). Following the initial observations of the comet (hereafter E3) P48/ZTF, the comet was observed by the Palomar 200-inch telescope, the Infrared Telescope Facility (IRTF), and the Palomar 60-inch telescope (P60) in order to characterize its physical properties. We will describe the P48 and the follow-up observations with the P200, P60, and IRTF in greater detail in the following section.

2 OBSERVATIONS

In addition to its all-sky coverage, the P48/ZTF scans the portions of the night sky within 60 of the Sun during nautical and astronomical twilight each morning and evening to search for Earth co-orbitals (Yeager & Golovich 2022, 2023), comets (Duev et al. 2021), Atira asteroids (asteroids with aphelia, 0.73 au $< Q <$ 0.98 au) and 'Ayló'chaxnim asteroids (asteroids that have aphelia $Q <$ 0.718 au, e.g. Bolin et al. 2021b, 2022a). On average, ∼500 sq. deg. is covered during each twilight session to a limiting r-band magnitude of ∼20 as described in section S1 of Bolin (2023). Each field is imaged 4–5 times with 30 s r-band exposures at an airmass of 2–2.5 with a spacing of ∼3–5 min between each field. A coverage map of the P48/ZTF pointings from 2022 February 11–2022 April 30 is presented in fig. S1 of Bolin (2023).

Between 2022 February and 2022 April, ∼100 000 sq. deg. of the sky was covered during evening and morning twilight by P48/ZTF as described in section S1 of Bolin (2023). E3 was discovered on 2022 March 2 in 5 x 30 s r-band P48/ZTF images taken at an airmass of ∼2.3 and seeing of ∼2 arcsec as measured in the images. A mosaic of the discovery detections of E3 are displayed in Fig. 1.

During the year following its discovery, E3 was routinely monitored for evolution in its activity (e.g. Jehin et al. 2022a, b, 2023). In early 2023 February, the comet came within 0.28 au of the Earth, reaching a peak visual magnitude of $V \sim 5$, providing an excellent opportunity to observe its coma and volatile contents in high detail. On 2022 Febraury 1, optical imaging of E3 was obtained with the P200 using the WaSP wide-field imager. A series of 8 x 45 s images in g band were taken when the comet was at an airmass of ∼1.1, the seeing was ∼2.2 arcsec as measured in the images, and the telescope was tracked at the motion of the comet (∼17 arcsec min^{-1}). Similar to the procedures described in Bolin et al. (2020b) and Bolin & Lisse (2020), the images were detrended and stacked on the motion of the comet. The composite image stack of E3 taken with the P200 is shown in Fig. 2.

The SpeX instrument on IRTF was used to obtain near-infrared spectra of E3 2023 February 26 when the comet was 0.85 au from the Earth and $V \sim 6.5$ as reported in observations submitted to the Minor Planet Centre.[1] The 0.8 x 15 arcsec slit was used providing an $R \sim 200$ spectrum of the comet between 0.7 and 2.5 μm. The comet was observed at an airmass of ∼1.7, and a nearby G-type star with

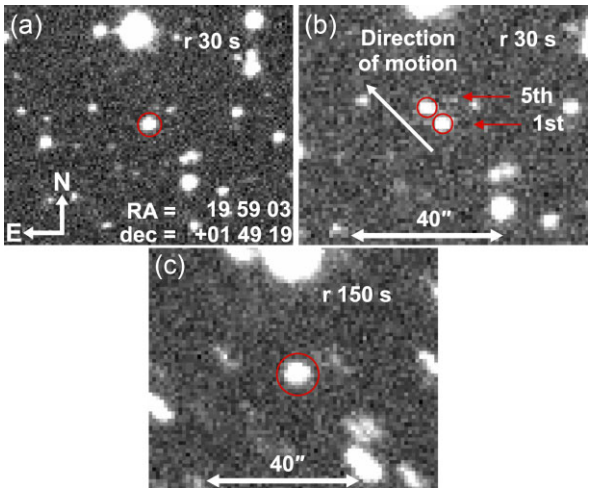

Figure 1. P48/ZTF images of E3 taken on 2022 March 2. Panel (A): the first of the five 30 s r-band P48/ZTF discovery images of E3 taken on 2022 March 2. The detection of E3 is encircled in red. Panel (B): composite image showing the position of E3 in the first and fifth of the five discovery images separated by ∼15 min. The images were aligned on the background stars before being coadded. The first and fifth images are labelled. The comet was moving ∼28 arcsec h^{-1} in the north-east direction separating the first and fifth detection of E3 by six arcsec. Panel (C): a composite stack of the detections of E3 in all five r-band images with an equivalent total exposure time of 150 s. The detection of E3 does not have an immediately apparent extended appearance, however, the measured FWHM of the comet's detection ∼3 arcsec compared to the ∼2 arcsec FWHM of nearby background stars of similar brightness. The cardinal directions are indicated in Panel (A). Panels (B) and (C) have the same orientation as in Panel (A). The spatial scale indicated in Panels (B) and (C) is the same as in Panel (A).

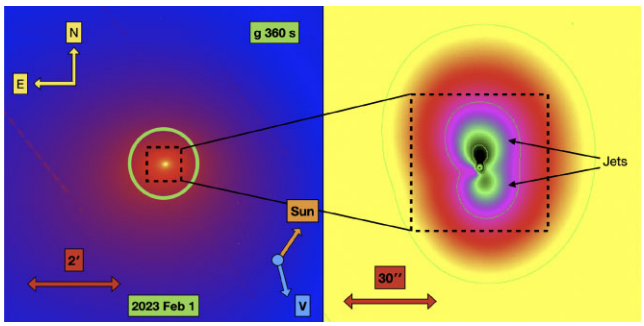

Figure 2. P200/WaSP g-band imaging of E3 taken on 2023 February 1. Left panel: a composite stack of 8 x 45 s g-band images of E3. The cardinal directions, solar direction, orbital motion direction, and image scale (2 arcmin ≃ 24 000 km at the 0.28 au distance of the comet) are indicated. A logarithmic colour scale is used where yellow corresponds to the brightest pixels and blue corresponds to the faintest pixels. Right panel: zoom in on the inner 45 arcmin nucleus region of E3 normalized by the distance from the optocentre to enhance features in the near-nucleus coma. The location of jet features are indicated with black arrows. A logarithmic colour scale is used where black corresponds to the brightest pixels and yellow corresponds to the faintest pixels.

[1] https://minorplanetcenter.net/db_search/show_object?utf8=&object_id = C%2F2022 + E3

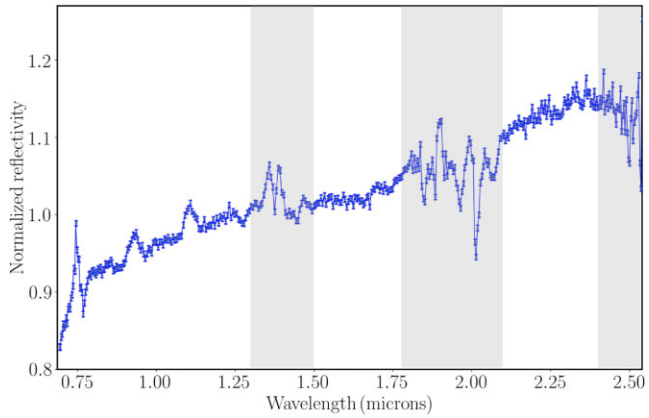

Figure 3. IRTF/SpeX near-infrared reflectance spectrum of E3 taken on 2023 February 26. The spectrum of E3 has been corrected for telluric features and for the solar spectrum by dividing it by a spectrum of a nearby solar analogue star and rebinned by a factor of two. The spectrum has been normalized to unity at 1.25 μm. The features at 0.75, 0.90, and 1.10 μm are caused by imperfect removal of telluric features. Regions in the spectrum with low atmospheric transparency are highlighted in grey (e.g. Avdellidou et al. 2022). The error bars correspond to 1-σ uncertainties and have been estimated by using the level of scatter in the spectrum (Holler et al. 2022). There is no sign of any water ice absorption feature at ∼1.5–1.6 μm (c.f., Yang, Jewitt & Bus 2009; Protopapa et al. 2014) down to the ∼ 1 per cent level.

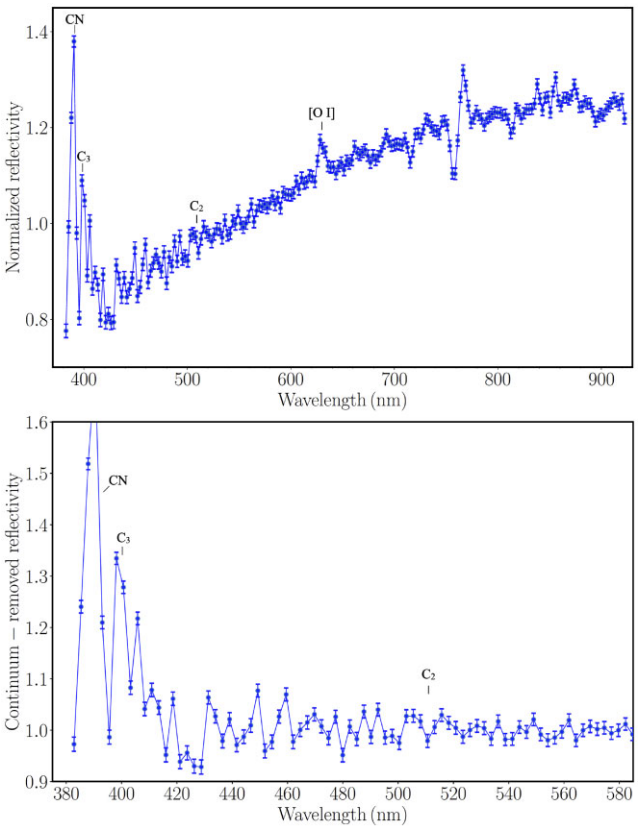

Figure 4. P60/SEDM visible spectroscopy of E3 on 2023 March 10. Top panel: visible reflectance spectrum of E3 taken with the P60/SEDM on 2023 March 10. The reflectance spectrum was computed by dividing the spectrum of E3 by a local solar analogue star to correct for telluric features and the solar spectrum. The spectrum has been normalized to unity at 550 nm. Bottom panel: a zoomed-in portion of the continuum-removed visible reflectance of E3. The error bars correspond to 1-σ uncertainties and have been estimated by using the level of scatter in the spectrum (Holler et al. 2022). The known locations of common cometary volatile species emissions detectable in visible spectra are indicated by small vertical black lines (Farnham, Schleicher & A'Hearn 2000). The lowness of the data point at 510 nm compared to adjacent bins may be due to a hot pixel.

colours similar to the Sun's was taken at a similar airmass as E3 to be used for telluric and slope correction (Lewin et al. 2020). The seeing was ∼1 arcsec as measured in the trace at 1.7 μm in the trace of the standard star.

Similar to the procedures described in Bolin et al. (2020a), the spectrum was taken as two ABBA sequences with each exposure possessing an equivalent exposure time of ∼135 s for a total integration time of 1080 s. The spectrum of E3 was extracted with a 2.4 arcsec wide trace and was divided by the solar analogue for telluric and slope correction resulting in the reflectance spectrum shown in Fig. 3.

The P60/ Spectral Energy Distribution Machine (SEDM) was used to observe E3 on 2023 March 10 when the comet was 1.21 au from the Earth and had a reported brightness of $V \sim 7.5$. A single 90 s exposure was taken at airmass 1.9 with 2.3 arcsec seeing measured in r-band image portion of the SEDM detector plane and a 7.5 arcsec extraction radius was used providing an $R \sim 100$ spectrum of the comet. Similar to the procedures described in Bolin et al. (2023c), a nearby G-type star was taken for telluric and slope correction. The G-type divided spectrum of E3 is presented in Fig. 3. A detailed description of the P48, P200, IRTF, and P60 observing circumstances is listed in table S2 of Bolin (2023).

3 RESULTS

3.1 Initial detection

C/2022 E3 was detected by P48/ZTF in 5 x 30 s r-band exposures taken in the morning twilight sky ∼44° from the Sun at 2022 March 2 (fig. S1 of Bolin 2023). Follow-up observations providing additional astrometry extending the orbital arc for E3 were taken by volunteers from the worldwide comet follow-up community (Bolin et al. 2022b). E3 had a slightly extended point spread function (PSF) with a full width at half-maximum (FWHM) of ∼3 arcsec in a composite stack of all 5 x 30 s r-band exposures compared to the FWHM of nearby background stars of ∼2 arcsec (panel C of Fig. 1). The extendedness of E3 was flagged as a possible comet by the Tails neural network trained to identify comets in P48/ZTF images taken on subsequent nights following the discovery (Duev et al. 2021). The activity of the comet was also reported by follow-up observers (Sato et al. 2022).

The combined set of observations of E3 including the P48/ZTF discovery images and the follow-up observations refined the orbit revealing that the comet has an eccentricity, e, of $\gtrsim$1, a perihelion distance, q, of ∼1.11 au (Fig. 5) and would reach perihelion on 2023 January 12 and approach within 0.28 au of the Earth in early 2023 February. A complete table of the parameters for the comet's orbital solution including observations taken between 2021 October and 2023 July are listed in table S1 of Bolin et al. (2023a).

The P200/WasP g-band images of E3 taken on February 1 show the near-nucleus environment of the comet's coma (Fig. 2). The images show the near-nucleus coma as having a width of ∼4 arcmin (∼50 000 km at the 0.29 au distance of the comet) and is offset from the nucleus in the anti-solar direction (left panel of Fig. 2). An enhanced version of the g-band image in the right panel of Fig. 2

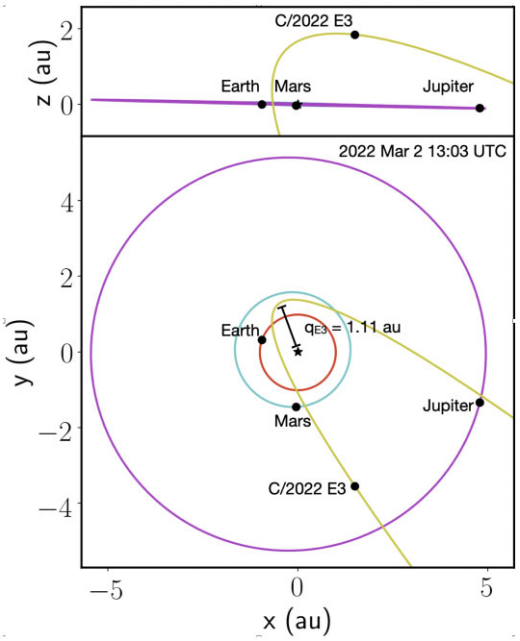

Figure 5. Orbital configuration of E3 and the inner Solar system on 2022 March 2. Top panel: a side view snapshot of the plane of the Solar system with the orbits and locations of Earth (red), Mars (blue), Jupiter (purple), and E3 (green) on 2022 March 2 are shown looking from the side. Bottom panel: the same as the top panel but looking from above the orbital plane of the inner Solar system. The perihelion distance of E3, q_{E3} is indicated. The heliocentric cartesian coordinates x, y, and z are indicated with the position of the Sun as the origin.

shows the presence of two jet-like structures in the image indicated with black arrows. One of the jet-like structures points north with a position angle of ∼0° and one points south with a position angle of ∼180°.

Both jet-like structures are as long as ∼20 arcsec (∼4 200 km at the 0.29 distance of the comet). The jet structures have a broad fan-like shape and may be due to cometary gases jetting from the nucleus as recent observations taken in narrow band comet gas filters have indicated the presence of significant amounts of CN, C_3, and C_2 in E3 (Jehin et al. 2022a, b, 2023). The wavelengths between 390 and 540 nm of the *g*-band filter (Fukugita et al. 1996) include the emission features from CN, C_3, and C_2 gases as well as the comet's dust continuum (Farnham et al. 2000). Therefore, the jet features seen in the *g*-band images may include both cometary gases and dust. However, similar jet-like structures have been detected in narrow-band filters with little dust contamination (Knight et al. 2023; Manzini et al. 2023).

The visible spectrographic observations of E3 were made using the P60/SEDM on 2023 March 10 show a reddish slope with colours at central wavelength locations equivalent to the central wavelength locations at *g* band (wavelength ∼470 nm), *r* band (wavelength ∼620 nm), *i* band (wavelength ∼750 nm), and *z* band (wavelength ∼900 nm) of g–r = 0.70 ± 0.01, r–i = 0.20 ± 0.01, and i–z = 0.06 ± 0.01 (top panel of Fig. 4). The optical colours of E3 are broadly consistent with the optical broad-band colour measurements of active comets made by ground-based surveys (e.g. g–r = 0.5 to 0.7, r–z = 0.2 to 0.5 Solontoi et al. 2012). The reddish trend seen in the visible SEDM spectrum continues into the near-infrared in the SpeX spectrum of E3 taken on on 2023 March 10. The E3 SpeX spectrum has colours at central wavelength locations equivalent to *z* band (wavelength ∼900 nm), *J* band (wavelength ∼1250 nm), *H* band (wavelength ∼1650 nm), and *K* band (wavelength ∼2200 nm) filters of z–$J = 0.90 \pm 0.01$, J–$H = 0.38 \pm 0.01$, and H–$K = 0.15 \pm 0.01$. The visible and near-infrared colours of E3 are significantly redder than the Sun's colours ($g_\odot$–$r_\odot = 0.46 \pm 0.01$, $r_\odot$–$i_\odot = 0.12 \pm 0.01$, $i_\odot$–$z_\odot = 0.03 \pm 0.01$, $z_\odot$–$J_\odot = 0.83 \pm 0.01$, $J_\odot$–$H_\odot = 0.35 \pm 0.01$, and $H_\odot$–$K_\odot = 0.05 \pm 0.01$, Willmer 2018).

The visible SEDM spectrum shows gas emission bands such as CN at ∼390 nm, C_3 at ∼400 nm, and C_2 at 510 nm as seen in the top and bottom panels of Fig. 4. The minimum value in the spectrum at 510 nm may be due to a hot pixel in the SEDM IFU. An emission feature possible is detected at ∼630 nm possibly corresponding to [O I]. However, this feature is likely blended with poorly subtracted telluric lines given the limited resolution of our spectrum (c.f., McKay et al. 2020).

Combining the fluorescence scattering efficiency factors for CN (Schleicher 2010), C_3 and C_2 (Cochran et al. 1992) with an optically thin Haser model (Haser 1957) to calculate gas production rates based on the scale lengths derived from (Cochran et al. 1992) and an outflow velocity of 0.5 km s^{-1} at 1 au (Cochran & Schleicher 1993). We numerically integrated the Haser model over the size of our SEDM aperture of 7.5 arcsec to find production rates for CN of $5.43 \pm 0.11 \times 10^{25}$ mol s^{-1}, C_3 of $2.01 \pm 0.04 \times 10^{24}$ mol s^{-1}, and C_2 of $3.08 \pm 0.5 \times 10^{25}$ mol s^{-1}. In addition, we calculated a value for A(0°)fρ, Afρ corrected to 0° phase angle (A'Hearn et al. 1984), of 1483 ± 40 cm based on the observed flux within the 7.5 arcsec radius used to extract the SEDM spectrum at ∼0.8 μm. Our gas production rates and A(0°)fρ value is similar to the gas production rates and A(0°)fρ calculated from independent observations of E3 taken around the same time as our observations (e.g. Jehin et al. 2023)

4 DISCUSSION AND CONCLUSION

E3 seems like an ordinary long-period comet with a red colour in the visible and near-infrared with common gas emission features seen in other comets entering the inner Solar system. The ratio of C_2/CN (∼0.6) is on the lower side compared to most Solar system comets with only ∼ 60 per cent having a higher C_2/CN ratio than E3 (A'Hearn et al. 1995). Comets with C_2/CN < 0.6 are considered to be depleted, with the majority of short-period comets, ∼ 40 per cent having C_2/CN < 0.6 (Cochran, Barker & Gray 2012). Long-period comets, on the other hand, are more likely to be non-depleted, with ∼ 80 per cent of long-period comets having C_2/CN < 0.6 (Cochran et al. 2012). Thus, while having a C_2/CN ratio that is relatively lower than most Solar system comets, E3 has a C_2/CN comparable to many other long-period comets. Additionally, the C_3/CN ($\sim 10^{-1.4}$) ratio is fairly typical compared to other Solar system comets which have C_3/CN $\sim 10^{-2}$ to 10^{-1} (A'Hearn et al. 1995). The value for A(0°)fρ of 1483 ± 40 cm is also comparable to other comets at similar solar distances of ∼1 au (∼10–10 000 cm, A'Hearn et al. 1995).

The discovery of E3 is surprising in the sense that its close approach with the Earth in 2023 January to 2023 March at solar elongations between 80 and 110° and near naked-eye brightness of $V \sim 5$ enabled detailed characterization of its volatile contents and physical properties at viewing geometries accessible to many ground and space-based observatories. The study of long-period comets that brighten dramatically as they pass near the Earth is new territory that will be enhanced by the opportunities for discovering fainter comets at farther heliocentric distances compared to contemporary surveys by near-future survey observatories such as Rubin Observatory's Legacy of Space and Time (Schwamb et al. 2023). Additionally, the

Comet Interceptor spacecraft mission will be designed to rendezvous with comets like E3 pairing well with the expected increasing flux of comet discoveries by future observational surveys (Marschall et al. 2022).

ACKNOWLEDGEMENTS

We wish to recognize and acknowledge the cultural role and reverence that the summit of Maunakea has always had within the indigenous Hawaiian community. The authors wish to recognize and acknowledge the cultural significance that Palomar Mountain has for the Pauma Band of the Luiseño Indians. Based on observations obtained with the Samuel Oschin Telescope 48-inch and the 60-inch Telescope at the Palomar Observatory as part of the Zwicky Transient Facility project. ZTF was supported by the National Science Foundation under Grants Nos. AST-1440341 and AST-2034437 and a collaboration including current partners. BTB was supported by an appointment to the NASA Postdoctoral Program at the NASA Goddard Space Flight Center, administered by Oak Ridge Associated Universities under contract with NASA.

DATA AVAILABILITY

The data underlying this article will be shared on reasonable request to the corresponding author. The ZTF Survey data from 2022 February to 2022 April are available in ZTF Public Data Release 12.

REFERENCES

A'Hearn M. F., Schleicher D. G., Millis R. L., Feldman P. D., Thompson D. T., 1984, AJ, 89, 579
A'Hearn M. F., Millis R. C., Schleicher D. O., Osip D. J., Birch P. V., 1995, Icarus, 118, 223
Avdellidou C. et al., 2022, A&A, 665, L9
Bellm E. C. et al., 2019, PASP, 131, 018002
Boe B. et al., 2019, Icarus, 333, 252
Bolin B. T., 2023, Supplemental Material
Bolin B. T., Lisse C. M., 2020, MNRAS, 497, 4031
Bolin B. T. et al., 2020a, AJ, 160, 26
Bolin B. T. et al., 2020b, ApJ, 900, L45
Bolin B. T. et al., 2021a, AJ, 161, 116
Bolin B. T. et al., 2021b, Minor Planet Electronic Circulars, 2021-V158
Bolin B. T. et al., 2022a, MNRAS, 517, L49
Bolin B. T. et al., 2022b, Minor Planet Electronic Circulars, 2022-F13
Bolin B. T. et al., 2023a, Supplemental Material
Bolin B. T., Ahumada T., Dokkum P. v., Fremling C., Hardegree-Ullman K. K., Purdum J. N., Serabyn E., Southworth J., 2023b, Icarus, 394, 115442
Bolin B. T., Noll K. S., Caiazzo I., Fremling C., Binzel R. P., 2023c, Icarus, 400, 115562
Bolin B. T. et al., 2023d, MNRAS, 521, L29
Bottke W. et al., 2023, Planet. Sci. J., 4, 168
Chang C.-K. et al., 2022, ApJ, 932, L5
Cochran A. L., Schleicher D. G., 1993, Icarus, 105, 235
Cochran A. L., Barker E. S., Ramseyer T. F., Storrs A. D., 1992, Icarus, 98, 151
Cochran A. L., Barker E. S., Gray C. L., 2012, Icarus, 218, 144
Duev D. A. et al., 2019, MNRAS, 486, 4158
Duev D. A. et al., 2021, AJ, 161, 218
Duncan M., Quinn T., Tremaine S., 1987, AJ, 94, 1330
Dybczyński P. A., Królikowska M., 2022, A&A, 660, A100
Farnham T. L., Schleicher D. G., A'Hearn M. F., 2000, Icarus, 147, 180
Farnocchia D. et al., 2022, Planet. Sci. J., 3, 156
Fukugita M., Ichikawa T., Gunn J. E., Doi M., Shimasaku K., Schneider D. P., 1996, AJ, 111, 1748
Golovich N., Lifset N., Armstrong R., Green E., Schneider M. D., Pearce R., 2021, preprint (arXiv:2104.03411)
Graham M. J. et al., 2019, PASP, 131, 078001
Haser L., 1957, Bull. Soc. R. des Sci. Liege, 43, 740
Holler B. J., Yanez M. D., Protopapa S., Young L. A., Verbiscer A. J., Chanover N. J., Grundy W. M., 2022, Icarus, 373, 114729
Jehin E., Vander Donckt M., Hmiddouch S., Manfroid J., Hutsemekers H., Moulane Y., 2022a, Astron. Telegram, 15491, 1
Jehin E., Donckt M. V., Manfroid J., Moulane Y., 2022b, Astron. Telegram, 15743, 1
Jehin E., Donckt M. V., Manfroid J., Hmiddouch S., Moulane Y., Jabiri A., Benkhaldoun Z., 2023, Astron. Telegram, 15973, 1
Klahr H., Schreiber A., 2020, ApJ, 901, 54
Knight M. M., Holt C. E., Villa K. M., Skiff B. A., Schleicher D. G., 2023, Astron. Telegram, 15879, 1
Lewin C. D., Howell E. S., Vervack Ronald J. J., Fernández Y. R., Magri C., Marshall S. E., Crowell J. L., Hinkle M. L., 2020, AJ, 160, 130
Manzini F., Oldani V., Ochner P., Bedin L. R., Reguitti A., 2023, Astron. Telegram, 15909, 1
Marschall R. et al., 2022, A&A, 666, A151
Masci F. J. et al., 2019, PASP, 131, 018003
McKay A. J., Cochran A. L., Dello Russo N., DiSanti M. A., 2020, ApJ, 889, L10
Oort J. H., 1950, Bull. Astron. Inst. Neth., 11, 91
Protopapa S. et al., 2014, Icarus, 238, 191
Purdum J. N. et al., 2021, ApJ, 911, L35
Sato H., Yoshimoto K., Guido E., Nakano S., 2022, CBET, 5111
Schleicher D. G., 2010, AJ, 140, 973
Schwamb M. E. et al., 2023, ApJS, 266, 22
Simon J. B., Blum J., Birnstiel T., Nesvorný D., 2022, preprint (arXiv:2212.04509)
Solontoi M. et al., 2012, Icarus, 218, 571
Vokrouhlický D., Nesvorný D., Dones L., 2019, AJ, 157, 181
Willmer C. N. A., 2018, ApJS, 236, 47
Yang B., Jewitt D., Bus S. J., 2009, AJ, 137, 4538
Yeager T., Golovich N., 2022, ApJ, 938, 9
Yeager T., Golovich N., 2023, preprint (arXiv:2302.11086)

SUPPORTING INFORMATION

Supplementary data are available at *MNRASL* online.

suppl_data

Please note: Oxford University Press is not responsible for the content or functionality of any supporting materials supplied by the authors. Any queries (other than missing material) should be directed to the corresponding author for the article.

This paper has been typeset from a TEX/LATEX file prepared by the author.